



Theoretical and experimental investigation of vibration-assisted scratching silicon

Weijie Wang^{a,*}, Guanghui Zhao^a, Yanling Tian^b, Zhilai Lu^c, Hui Tang^d, Fujun Wang^a, Dawei Zhang^a

^a Key Laboratory of Mechanism Theory and Equipment Design of Ministry of Education, Tianjin University, Tianjin, 300072, PR China

^b School of Engineering, University of Warwick, Coventry, CV4 7AL, UK

^c State Key Laboratory of High Performance Complex Manufacturing, Central South University, Changsha, 410083, PR China

^d State Key Laboratory of Precision Electronic Manufacturing Technology and Equipment, Guangdong University of Technology, Guangzhou, 510006, PR China



ARTICLE INFO

Keywords:

Vibration-assisted tip based nanofabrication
Single-crystal silicon
Cutting force
Force model
Nanomachining process

ABSTRACT

Interaction between tip and workpiece plays a crucial role in determining the scratching depth in Vibration-assisted Tip Based Nanofabrication (VTBN), which is more complicated than that of conventional scratching (without vibration-assisted). To establish the relationship between the scratching depth and machining parameters, a cube-corner indenter is employed to conduct VTBN procedure. The indenter is simplified as a cone to calculate the contact model in both 1D groove and 2D surface machining processes. An instantaneous normal load model is established based on the developed tip-workpiece contact model. Due to the variation of instantaneous contact area, effective contact area is put forward for the first time to predict the normal load. Effects of vibration frequency and amplitude on the normal load and surface quality are analyzed based on the proposed model. Experimental results show that higher frequency and larger amplitude will reduce the effective contact area. Vibration can increase the scratching depth and width without enlarging the cutting force. Furthermore, the inconsistency caused by scratching directions in conventional scratching is also overcome during VTBN.

1. Introduction

Semiconductors with nanostructures have a wide application in various fields such as physics, aerospace, biological and chemistry [1–3]. Many technologies including Focused Ion Beam (FIB) [4], Electron Beam (EB) [5], reactive-ion etching [6], and Tip Based Nanofabrication (TBN) [7] have been developed to fabricate micro/nano structures. Among them, TBN has been extensively studied for its advantages of low cost and high accuracy especially in Vibration-assisted Tip Based Nanofabrication (VTBN) [8]. VTBN is capable to fabricate micro/nano structures with higher efficiency and smaller cutting force [9]. But the control of scratching depth during VTBN is still a mystery due to its complication and the limitation of experimental technologies.

Molecular dynamic (MD) is the most used numerical method to study VTBN process. The effect of vibration parameters has been studied on different semiconductors during VTBN process via MD [10–12]. Zheng et al. compared the effect of one-dimensional and two-dimensional vibration in scratching [13]. It turns out that vibration-assisted scratching can reduce the total force which is advantageous in scratching.

Two-dimensional vibration turned out to have a better performance than one dimensional vibration [14]. Chen et al. also utilizes MD simulation to study the surface damage, the interactions of dislocations become more intense and accelerate the annihilation of dislocations [15]. Besides, Finite Element Method (FEM) is also employed to study the effect of vibration parameters [16–18]. However, numerical simulation cost too much computing resources to replicate the dimension scale of actual experiments.

In addition to numerical simulation, experimental methods were also employed to reveal the relationship between scratching depth and cutting parameters. Versen et al. fabricated nanostructures on GaAs in the tapping mode of an atomic force microscope [19]. Grooves of different depth were obtained by adjusting scanning parameters. Iwata et al. found that the bottom of groove is obvious flatter with the oscillating tip than non-oscillating tip, further substantiating the advantage of VTBN [20]. Lu et al. studied the effect of several key vibration parameters on scratching depth and using a polynomial function to describe their relationship. Frequency, amplitude, and vibration model were proved to be dominant [21]. Li et al. studied the effect of feed rate and amplitude in vibration-assisted grinding [22]. The force model was fitted using

* Corresponding author.

E-mail address: wangweijie@tju.edu.cn (W. Wang).

Nomenclature

F_v	normal load
H	hardness
A_z	normal contact area
z	height of the cross-section
R	radius of the cross-section
A	amplitude of vibration
ω	angular velocity
t	machining time
h_m	cutting depth
h_r	residual depth
h_R	height of the spherical crown
θ	rotation angle
θ_t	half cone angle

$\theta_1 \theta_2 \theta_3$	value of θ at several particular positions
r	tip radius
(T_x, T_y, T_z)	coordinate of tip
T	vibration period
T_{1s}	coordinate of T_1 in $X_sO_sY_s$
T_{2s}	coordinate of T_2 in $X_sO_sY_s$
T_{1t}	coordinate of T_1 in $X_tO_tY_t$
T_{2t}	coordinate of T_2 in $X_tO_tY_t$
Δ	feed step
h_2	depth difference of first two grooves
$A_{\text{effective}}$	effective normal contact area
E	elastic modulus
σ	poisson's ratio
θ_f	face angle of indenter

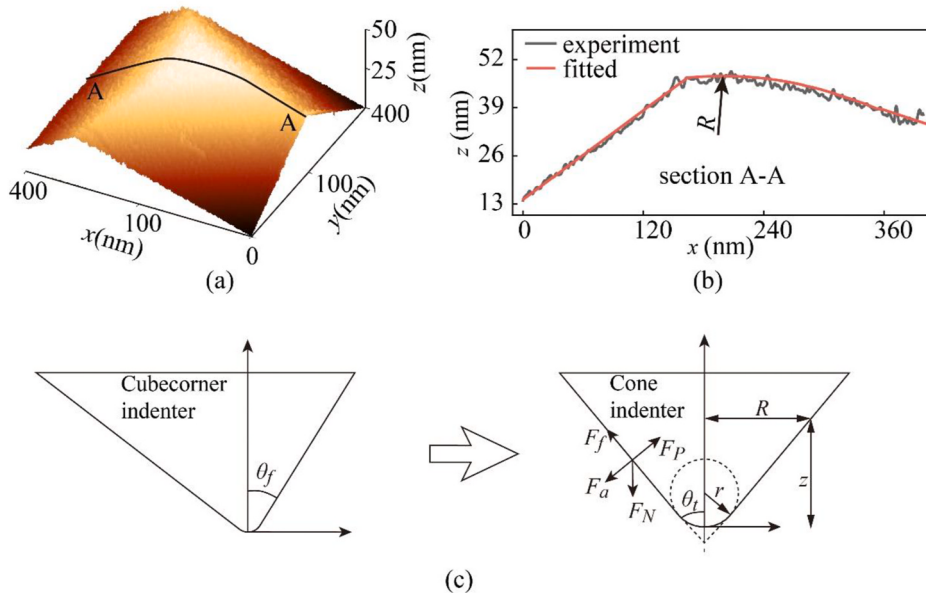


Fig. 1. (a) AFM scanning image of indenter tip, (b) profile of section A-A, (c) conversion from cubecorner indenter to conical indenter.

genetic algorithm. Similar methods were also employed by other scholars [23,24]. But their methods need numerous experiments to improve the prediction accuracy and cannot reveal the mechanism of material removal behavior in VTBN.

Due to the limitation of those above methods, many scholars endeavored to establish the theoretical model of scratching depth and vibration parameters. Traditional ultrasonic vibration-assisted milling process controls the machining depth and surface roughness mainly by kinematic trajectory [25,26]. However, due to the low rigidity of fabrication system, VTBN process modifies machined surface via controlling cutting force. Cao et al. established an instant cutting force model of vibration-assist scratching process [27]. The system has a quite high stiffness as the cutting tool is mounted directly at the rail end. The position of cutting tools is pre-defined by the program. The feature dimension is mainly determined by the position of cutting tool and workpiece. While scratching force cannot be used to control feature dimension. Such limitation also exists in other researches [28]. But in some other applications, cantilever is relative flexible and scratching depth is mainly controlled by scratching force and vibration parameters. Jiao et al. calculated the removal material volume in VTBN, but scratching force is not calculated [29]. Geng et al. modeled the peak

force in VTBN based on the force-distance curve [30]. Similar method was also adopted in another research [31]. But the cantilever works around its resonant frequency, making it difficult to adjust the dimension of fabricated feature. In addition, this method only works when the vibration contains a z-component. To predict the scratching depth, Heamawatanachai et al. established a force model of VTBN [32]. A conical tip is used to fabricate nano grooves and normal force is predicted in a single turn. But variation of scratching force is relative smooth due to the low rigidity of cantilever. Wang et al. adopt a similar method to predict scratching depth [33]. Predicted depth varies from tens of nanometers to hundreds of nanometers while experimental depth is a constant. Besides, their models are built for scratching a single groove and cannot be used when scratching 2-dimensional planes. To sum up, current models cannot predict scratching depth precisely in VTBN, there is still a lack of effective models.

This paper aims to establish a theoretical model of scratching depth and force in VTBN and reveal the relationship between scratching force, depth, and vibration parameters in machining both 1-D grooves and 2-D planes. A simplified tip model and corresponding normal load model is established in section 2. Detailed experiment setup is introduced in section 3. Theoretical analysis and experiment results is discussed in

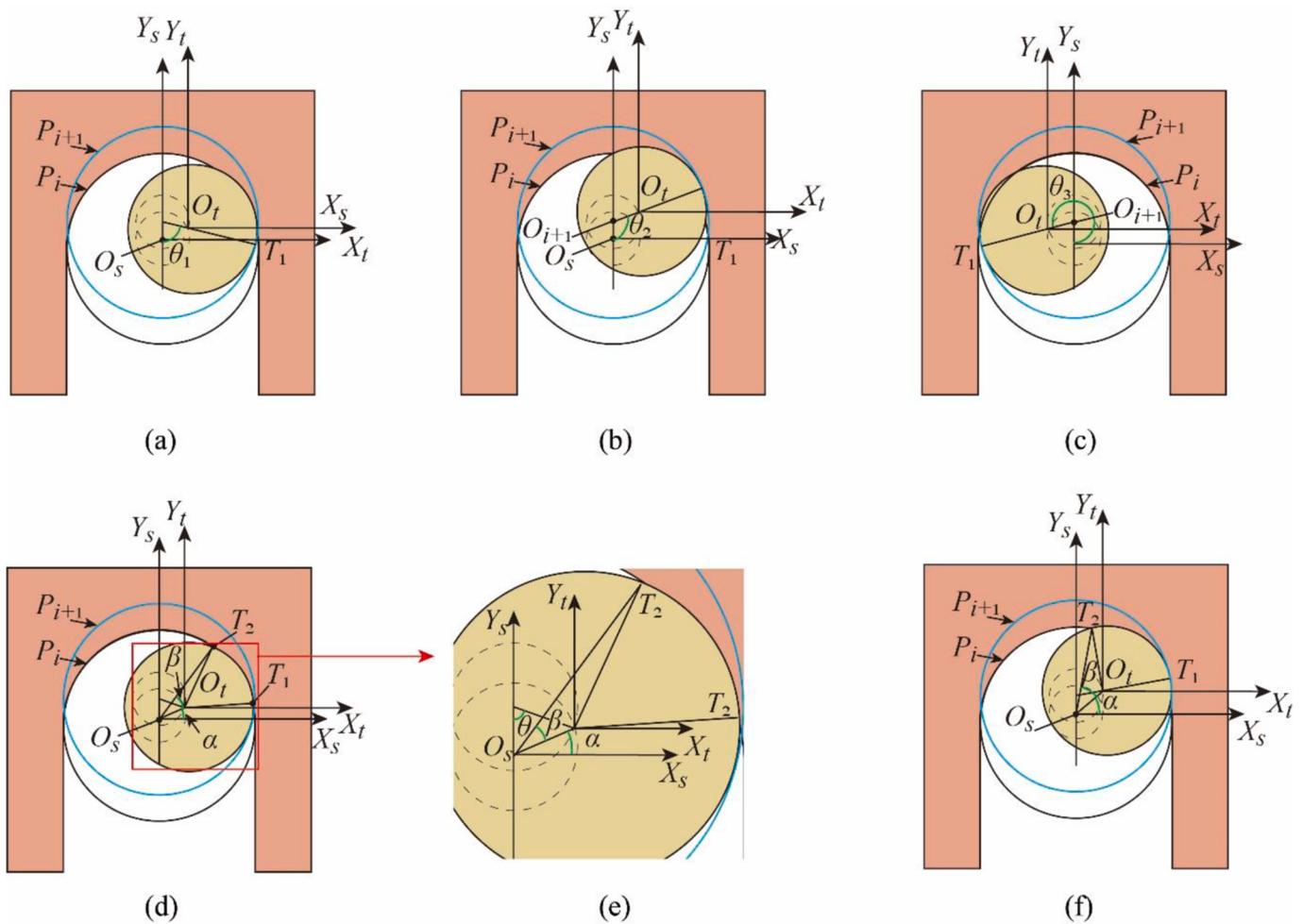


Fig. 2. Schematic diagram of scratching single groove surface, (a) critical position in single groove scratching ($\theta = \theta_1$), (b) critical position in single groove scratching ($\theta = \theta_2$), (c) critical position in single groove scratching ($\theta = \theta_3$), (d) planar view of first stage in single groove scratching, (e) local enlarged view of first stage in single groove scratching. (f) planar view of second stage in single groove scratching.

section 4. The conclusion is summarized in section 5.

2. Normal load model

In this section, a force prediction model was established in scratching a single groove first. Then, the model was extended to a 2D surface machining process. Nano scratching process can be considered as a hard abrasive scratching on a relative soft substrate. According to Tabor's theory [34], normal load (F_v) in nano scratching can be expressed as following equation:

$$F_v = HA_z \quad (1)$$

where H and A_z represents the hardness of substrate and normal contact area between tip and workpiece. In a conventional scratching process (without vibration assisting), A_z is depended on elastic recovery and cutting depth, which can be considered as a constant when normal load is stable. But in VTBN process, tip trajectory consists of a vibration trajectory and a linear motion trajectory, while contact area will change with the vibration trajectory every moment. Trajectory of tip in Cartesian coordinate (T_x, T_y, T_z) can be expressed as following equation (T_z is depend on the cutting depth.):

$$\begin{cases} T_x = A \sin(\omega t) \\ T_y = A \cos(\omega t) + vt \\ T_z = h_m \end{cases} \quad (2)$$

where A is the amplitude of vibration trajectory, which is a constant in machining process, ω is angular velocity of vibration, t is machining time, v is scratching speed, h_m is cutting depth. Thus, A_z can be expressed as follows:

$$A_z = f(h_m, \theta, A) \quad (3)$$

where h_m is cutting depth, $\theta = \omega t$. The key is to establish the function of A_z , which will be the focus of next section.

2.1. Tip model

Tip geometry has a significant influence on contact area. To establish the tip geometry model, tip topography was scanned by an AFM, which has a three sides pyramid with a spherical crown, as shown in Fig. 1 (a). Profile of section A-A is shown in Fig. 1 (b). Tip radius is fitted to be about 200 nm. In order to reduce the model complication, it is necessary to adopt some simplification of the indenter tip. According to Wang et al. [33], the tip is simplified as a cone base and a spherical crown, as shown in Fig. 1 (c). The transform principle is to keep the area of cross-section identical in the same depth. Geometric parameters of simplified tip model can be calculated by Eq. (4)~(6)

$$\theta_t = \arctan \left(\sqrt{\frac{3\sqrt{3}\tan^2\theta_f}{\pi}} \right) \quad (4)$$

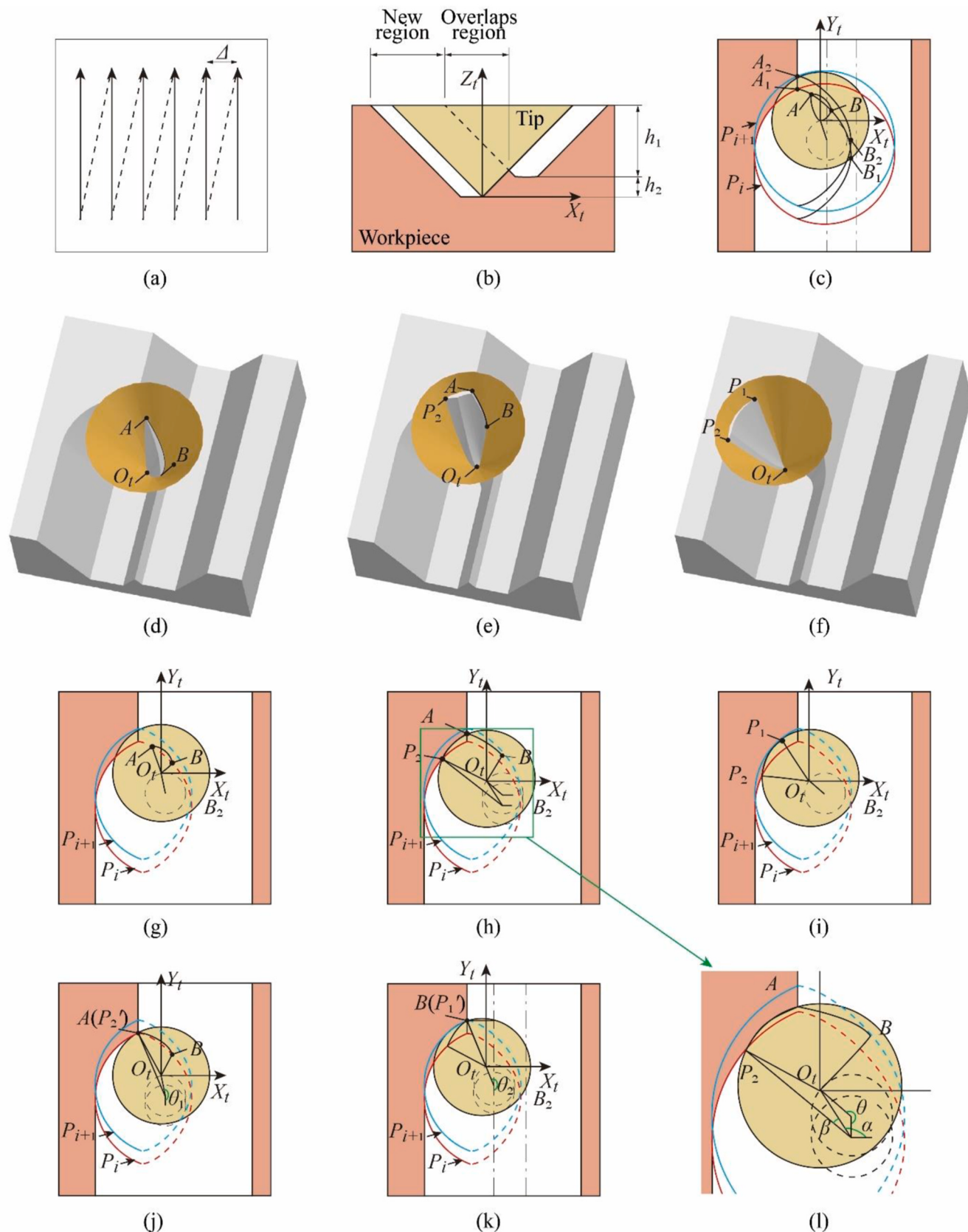


Fig. 3. Schematic diagram of scratching 2D surface, (a) tip trajectory of 2D scratching; (b) front view of 2 adjacent grooves, (c) top view of 2 adjacent grooves, (d) 3D view of first stage in 2D surface scratching, (e) 3D view of second stage in 2D surface scratching, (f) 3D view of third stage in 2D surface scratching, (g) planar view of first stage in 2D surface scratching, (h) planar view of second stage in 2D surface scratching, (i) planar view of third stage in 2D surface scratching, (j) planar view of critical position between first and second stage, (k) planar view of critical position between second and third stage, (l) local enlarged view of second stage in 2D scratching.

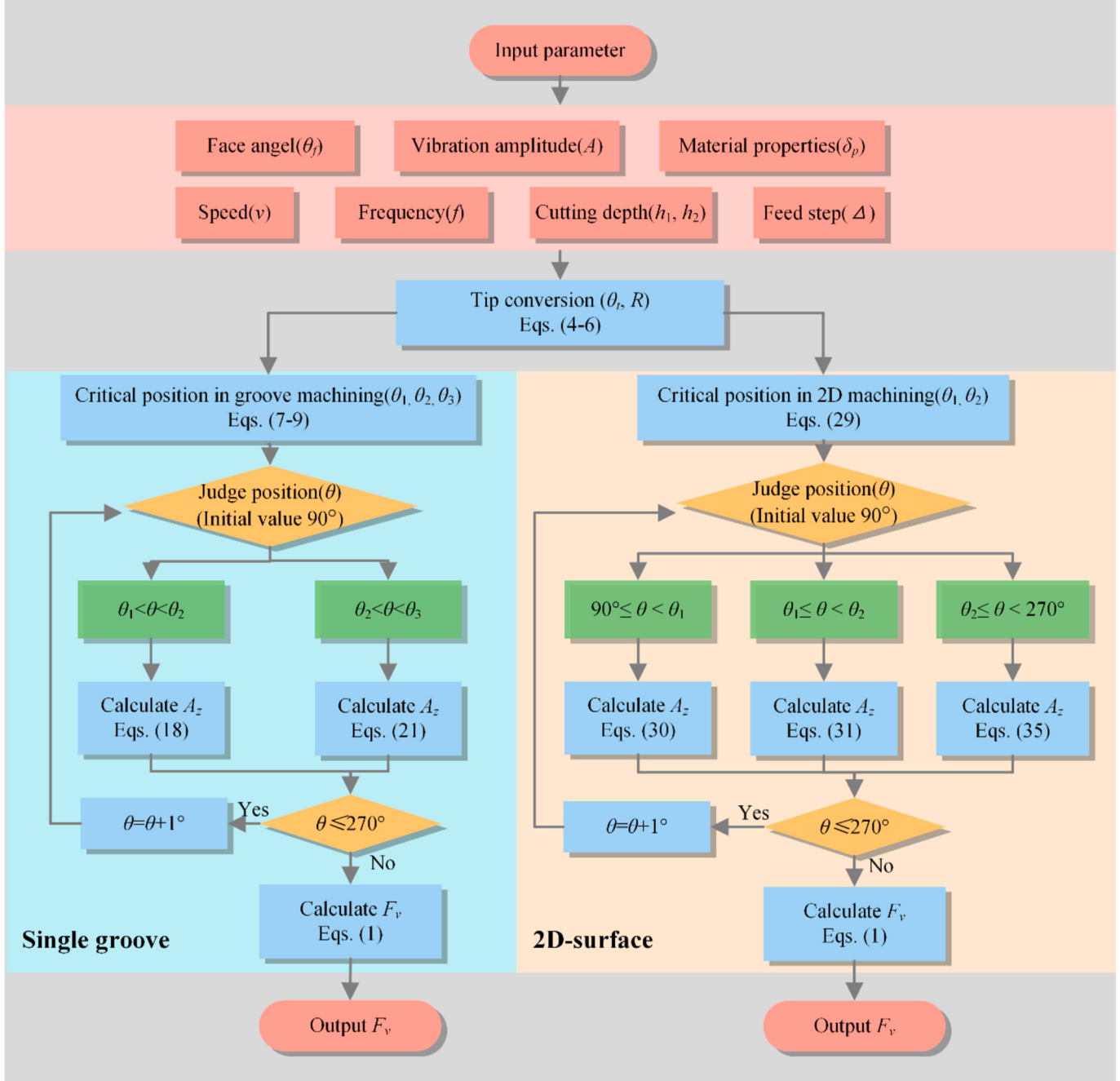


Fig. 4. Flow chart of depth prediction model in VTBN.

$$h_R = r(1 - \sin \theta_t) \quad (5)$$

where θ_t is the half cone angle, θ_f is the face angle of cubecorner tip, h_R is the height of spherical crown, r is the tip radius, respectively. Radius of contact area can be expressed as follows [32]:

$$R = \begin{cases} \sqrt{r^2 - (r^2 - h_m^2)}, & 0 < z \leq h_R \\ (h_m - h_R) \tan \theta_t + r \cos \theta_t, & z > h_R \end{cases} \quad (6)$$

where R is the radius of cross-section at the depth of h_m .

2.2. Contact model in 1D groove scratching

Tip trajectory in two vibration periods is shown in Fig. 2 (a) ~ (c). Boundary in current period (P_i) and next period (P_{i+1}) is represented by

solid black lines and solid blue lines respectively, which are considered as two circles. Rotation center of P_i and P_{i+1} is indicated by point O_s and O_{i+1} respectively. Coordinate $X_t O_t Y_t$ is fixed on indenter and origin is coincident with indenter tip. Coordinate $X_s O_s Y_s$ is fixed on rotation center. Angel between $O_s O_t$ and $X_s O_s$ is represented by θ , as shown in Fig. 1 (d) and (e). Process of P_{i+1} period goes in the following procedure, first, indenter contact the machined surface of P_i period and cutting process begins, but the indenter didn't reach the boundary of P_{i+1} period in this stage. The value of θ is denoted by θ_1 at the beginning of current position, which is shown in Fig. 1 (a). Then, the indenter keeps moving until it contacts the boundary of P_{i+1} period, the machined surface of P_{i+1} period is formed in this stage. The value of θ is denoted by θ_2 when this stage begins, which is shown in Fig. 1 (b). The third stage begins when indenter moves backward and no longer contacts the machined surface, machining process is considered complete in P_{i+1} period. The

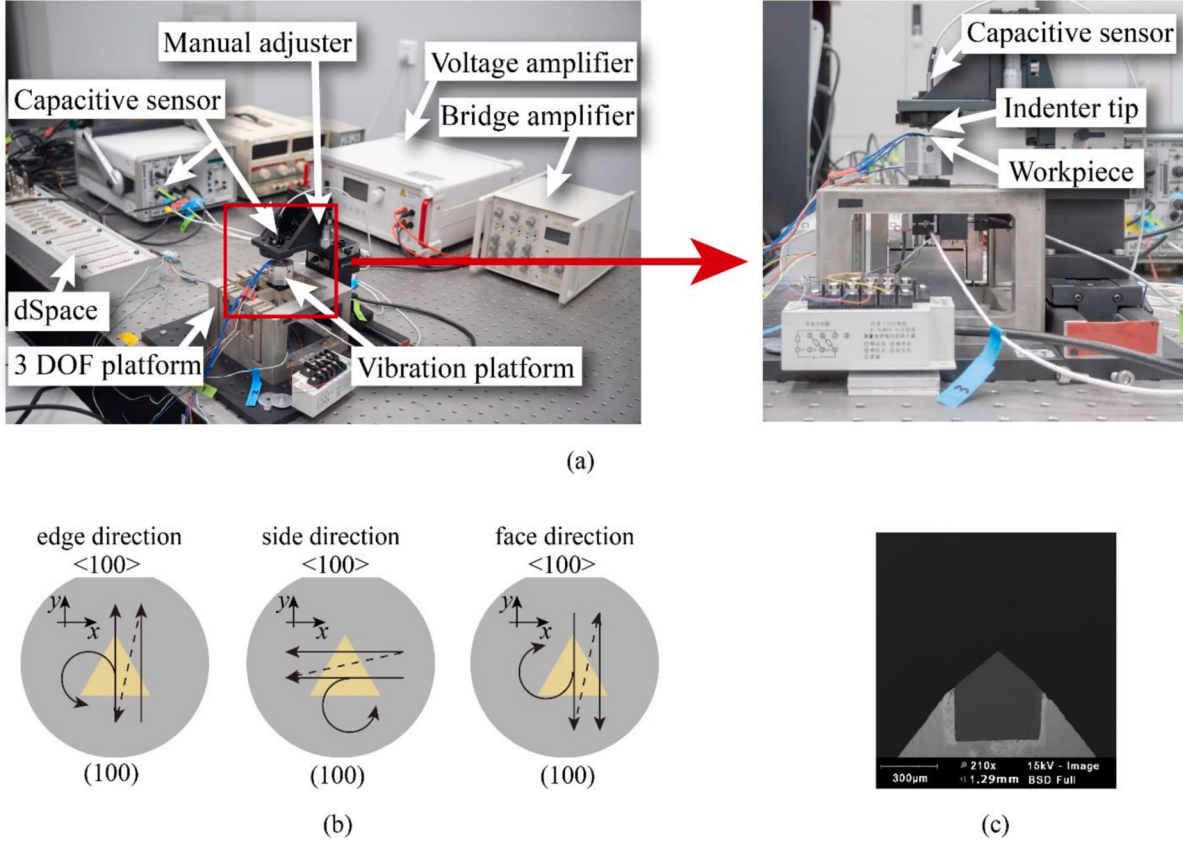


Fig. 5. (a) Experiment setup, (b) Scratching and vibration directions, (c) SEM image of indenter tip.

value of θ is denoted by θ_3 in the beginning of the third stage, as shown in Fig. 1 (c). The interaction between indenter tip and groove surface is neglected in the third stage. $\theta_1, \theta_2, \theta_3$ can be calculated by the following equations:

$$\theta_1 = \arccos\left(\frac{vT}{2A}\right) \quad (7)$$

$$\theta_2 = \arccos\left(\frac{vT}{2(A+R)}\right) \quad (8)$$

$$\theta_3 = 2\pi - \theta_2 \quad (9)$$

where T is the vibration period. Normal contact area will be calculated in first and second stage separately.

When θ is between θ_1 and θ_2 , scratching process is in the first stage, as shown in Fig. 2 (d), contact area is indicated by $O_t T_1 T_2$. Edge $O_t T_1$ and $O_t T_2$ is considered as straight line. Indenter contacts with the machined groove boundary at point T_1 and T_2 . Positions of T_1 and T_2 in coordinate $X_s O_s Y_s$ can be expressed as follows:

$$T_{1s} = \begin{bmatrix} (A+R)\sin(\alpha - \beta) \\ -(A+R)\cos(\alpha - \beta) \\ z \end{bmatrix} \quad (10)$$

$$T_{2s} = \begin{bmatrix} (A+R)\sin(\alpha + \beta) \\ -(A+R)\cos(\alpha + \beta) \\ z \end{bmatrix}$$

where α is the position angle of indenter tip, β is the angle of OT_2 and $O_s O_t$ as shown in Fig. 2 (e). α and β can be expressed as follows [33]:

$$\alpha = \arctan\left(\frac{vT - A \cos \theta}{A \sin \theta}\right) \quad (11)$$

$$\beta = \arccos\left(\frac{|OO_t|^2 + (A+R)^2 - R^2}{2|OO_t|(A+R)}\right) \quad (12)$$

where $O_s O_t$ can be calculated by following equation:

$$|O_s O_t| = \sqrt{v^2 T^2 + A^2 - 2vTA \cos \theta} \quad (13)$$

In order to calculate the normal contact area, the positions of T_1 and T_2 need to be transformed to the $X_t O_t Y_t$ coordinate system. Transformation matrix is expressed as follows:

$$R_T = \begin{bmatrix} 1 & 0 & 0 & -A \sin \theta \\ 0 & 1 & 0 & A \cos \theta - vT \\ 0 & 0 & 1 & 0 \\ 0 & 0 & 0 & 1 \end{bmatrix} \quad (14)$$

Thus, position of T_1 and T_2 in coordinate $X_t O_t Y_t$ can be calculated as:

$$\begin{bmatrix} T_{1t} \\ 1 \end{bmatrix} = R_T \cdot \begin{bmatrix} T_{1s} \\ 1 \end{bmatrix} \quad (15)$$

$$\begin{bmatrix} T_{2t} \\ 1 \end{bmatrix} = R_T \cdot \begin{bmatrix} T_{2s} \\ 1 \end{bmatrix} \quad (16)$$

where T_{1t} and T_{2t} are the coordinate of T_1 and T_2 in $X_t O_t Y_t$ coordinate system. The expression of $O_t T_1$ and $O_t T_2$ with respect to $X_t O_t Y_t$ coordinate system can be derived as:

$$\begin{aligned} O_i T_{1t} : ((A + R)\cos(\alpha - \beta) - A \cos \theta + vT)x + ((A + R)\sin(\alpha - \beta) - A \sin \theta)y = 0 \\ O_i T_{2t} : ((A + R)\cos(\alpha + \beta) - A \cos \theta + vT)x + ((A + R)\sin(\alpha + \beta) - A \sin \theta)y = 0 \end{aligned} \quad (17)$$

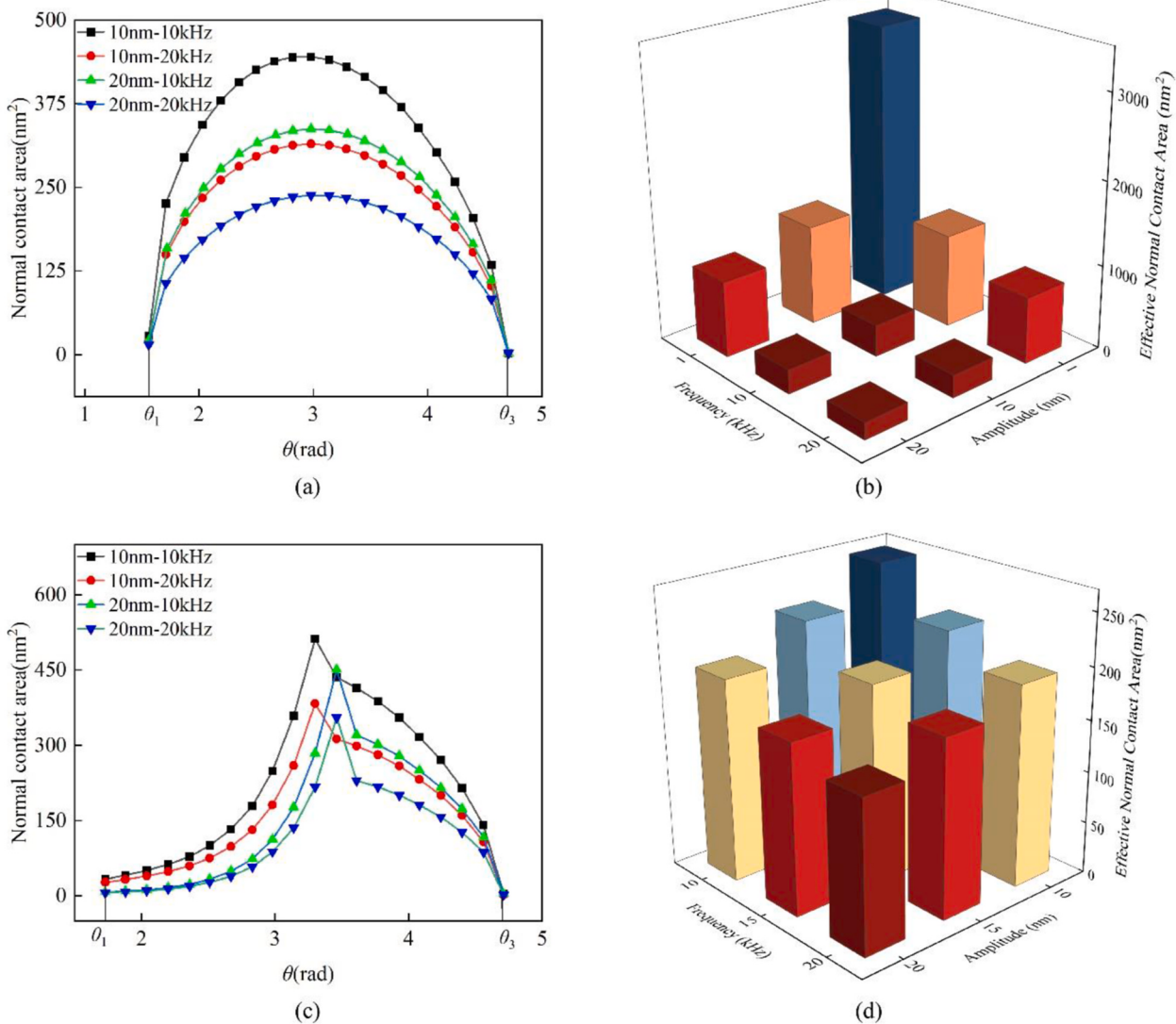


Fig. 6. Simulation results of (a) Instantaneous contact area of different vibration parameters in 1D groove machining, (b) Effective contact area of different vibration parameters in 1D groove machining, (c) Instantaneous contact area of different vibration parameters in 2D surface machining, (d) Effective contact area of different vibration parameters in 2D surface machining.

Table 1

Scratching parameters in force model validation experiments.

Experiment	Speed (v)	Feed (Δ)	Normal load (F _v)	Amplitude (A)	Frequency (f)
Groove	3 μm/s	–	10 μN	20 nm	20 kHz
2D surface	3 μm/s	50 nm	10 μN	20 nm	20 kHz

The normal contact area can be calculated by integrating area $O_1 T_2$, which is shown below:

$$\begin{aligned} A_z = & \int_{T_{1y}}^{T_{2y}} \sqrt{R^2 - y^2} dy - \int_0^{T_{2y}} \frac{(A + R)\sin(\alpha + \beta) - A \sin \theta}{-(A + R)\cos(\alpha + \beta) + A \cos \theta - vT} y dy \\ & + \int_0^{T_{1y}} \frac{(A + R)\sin(\alpha - \beta) - A \sin \theta}{-(A + R)\cos(\alpha - \beta) + A \cos \theta - vT} y dy \end{aligned} \quad (18)$$

When θ is between θ_2 and θ_3 , scratching process is in the second stage, as shown in Fig. 2 (e), contact area is indicated by $O_i T_1 T_2$. T_1 lies on the boundary of P_{i+1} period and T_2 lies on the boundary of P_i period. Position of T_1 and T_2 in coordinate $X_t O_t Y_t$ can be expressed as follows:

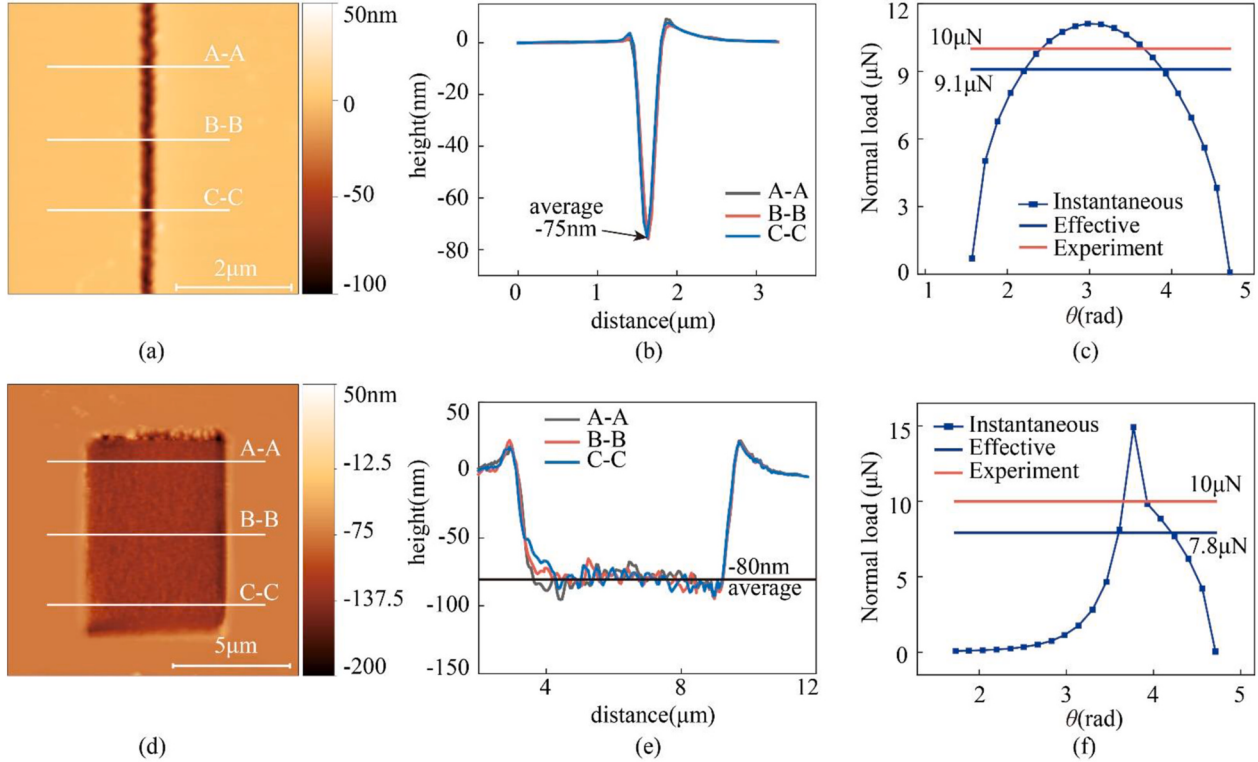


Fig. 7. Experiment results (a) single groove result, (b) extracted section profile of groove, (c) theoretical and experimental normal load during surface machining, (d) 2D surface result, (e) extracted section profile of surface, (f) theoretical and experimental normal load during surface machining.

$$\begin{aligned} T_{1t} &= \begin{bmatrix} R \sin \theta \\ -R \cos \theta \\ z \end{bmatrix} \\ T_{2t} &= \begin{bmatrix} (A + R)\sin(\alpha + \beta) - A \sin \theta \\ -(A + R)\cos(\alpha + \beta) + A \cos \theta - vT \\ z \end{bmatrix} \end{aligned} \quad (19)$$

The expression of $O_t T_1$ and $O_t T_2$ with respect to $X_t O_t Y_t$ coordinate system can be derived as:

2.3. Contact model in 2D surface scratching

A 2D surface can be obtained by repeating the 1D groove scratching process with a constant feed step which is perpendicular to the scratching direction. Trajectory of indenter is in a zigzag shape, feed step is represented by Δ , which is shown in Fig. 3 (a). In order to calculate the contact area of second groove, a detail schematic diagram of two adjacent grooves is shown in Fig. 3 (b) and (c), where h_1 is the cutting depth of first groove and h_2 is the difference between first and second groove cutting depth. h_2 is zero for a flat 2D surface. Unmachined area is filled in red color and machined groove is blank. Boundary of previous period

$$\begin{aligned} O_t T_1 : \cot \theta x + y = 0 \\ O_t T_2 : ((A + R)\cos(\alpha + \beta) - A \cos \theta + vT)x + ((A + R)\sin(\alpha + \beta) - A \sin \theta)y = 0 \end{aligned} \quad (20)$$

The normal contact area can be calculated by integrating area $OT_1 T_2$. But T_{1y} and T_{2y} may be a negative value when $\theta_2 < \theta < 90^\circ$ or $270^\circ < \theta < \theta_3$, integration will be performed in two regions separately. Thus, normal contact area can be expressed as:

(P_i) and current period (P_{i+1}) are indicated by red and blue lines respectively. Overlaps region is defined as the machined area of previous grooves which will be removed again in current groove, while the rest of current groove is defined as new region, which is shown in Fig. 3 (b). Machining Processing of P_{i+1} period is in the following procedure which

$$\left\{ \begin{array}{l} A_z = \int_{T_{1y}}^{T_{2y}} \sqrt{R^2 - y^2} dy + \int_0^{T_{1y}} (-\tan \theta) y dy + \int_0^{T_{2y}} \frac{(A + R)\sin(\alpha + \beta) - A \sin \theta}{-(A + R)\cos(\alpha + \beta) + A \cos \theta - vT} y dy \quad \theta_2 < \theta < 90^\circ \text{ or } 270^\circ < \theta < \theta_3 \\ A_z = \int_{T_{1x}}^{T_{2x}} \sqrt{R^2 - x^2} dx - \int_0^{T_{1x}} (-\cot \theta) x dx + \int_0^{T_{2x}} \frac{-(A + R)\cos(\alpha + \beta) + A \cos \theta - vT}{(A + R)\sin(\alpha + \beta) - A \sin \theta} x dx \quad 90^\circ < \theta < 270^\circ \end{array} \right. \quad (21)$$

Table 2

Scratching parameters in model applicable investigate experiments.

Group Nos.	Speed (v)	Normal load (F_v)	Amplitude (A)	Frequency (f)
1	3 $\mu\text{m}/\text{s}$	10 μN	3	1,3,5,10,20,25 (kHz)
2	3 $\mu\text{m}/\text{s}$	10 μN	3,5,10,13,16,20 (nm)	5

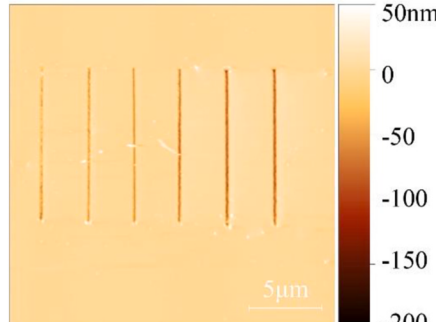
is shown in Fig. 3 (c) ~ (e). In the first stage, indenter contact the machined surface of P_i period, and cutting process began. Only the overlaps region is removed in this stage, as shown in Fig. 3 (d) and (g). Then, indenter keeps moving until it contacts the new region, the intersection of tip surface and boundary of P_i period is denoted by P_2 . Indenter contacts both the overlaps region and new region in this stage, as shown in Fig. 3 (e) and (h). In the third stage, indenter only contact new region as shown in Fig. 3 (f) and (i). Normal contact area will be discussed accordingly. Coordinate $X_tO_tY_t$ is fixed with indenter, where O_t coincides with indenter tip. Coordinate $X_sO_sY_s$ is fixed with rotation center of P_{i+1} period. The transformation matrix $T_{S \rightarrow T}$ for transforming a point from $X_sO_sY_s$ to $X_tO_tY_t$ can be expressed as follows:

$${}^tO_t = {}^sO_t + T_{S \rightarrow T} = \begin{bmatrix} A \sin \theta \\ -A \cos \theta \\ h_2 \end{bmatrix} + \begin{bmatrix} -A \sin \theta \\ A \cos \theta \\ -h_2 \end{bmatrix} \quad (22)$$

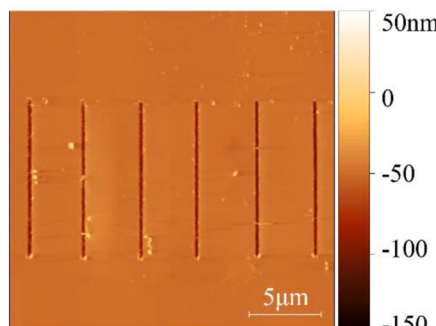
where tO_t , sO_t represent the coordinate of O_t in $X_tO_tY_t$ and $X_sO_sY_s$ frame respectively. Expression of overlaps region in coordinate $X_tO_tY_t$ can be expressed as follows:

$$z = -\cot \theta_t (x - (\Delta_t - A - A \sin \theta)) \quad (23)$$

where $\Delta_t = \Delta + h_2 \tan \theta_t$. Surface of indenter in $X_tO_tY_t$ coordinate system



(a)



(c)

can be expressed as follows:

$$\begin{cases} x^2 + y^2 = R^2 \\ z = R \cot \theta_t \end{cases} \quad (24)$$

AB represents the intersection of overlaps region and indenter surface, which can be obtained by solving Eqs. (23) and (24). Trajectory boundary of P_i period and P_{i+1} period in different coordinates can be expressed as follows:

$$X_tO_tY_t \begin{cases} P_i : (x + A \sin \theta)^2 + (y - A \cos \theta + vT)^2 = (R + A)^2 \\ P_{i+1} : (x + A \sin \theta)^2 + (y - A \cos \theta)^2 = (R + A)^2 \end{cases} \quad (25)$$

$$X_sO_sY_s \begin{cases} P_i : x^2 + (y + vT)^2 = (R + A)^2 \\ P_{i+1} : x^2 + y^2 = (R + A)^2 \end{cases} \quad (26)$$

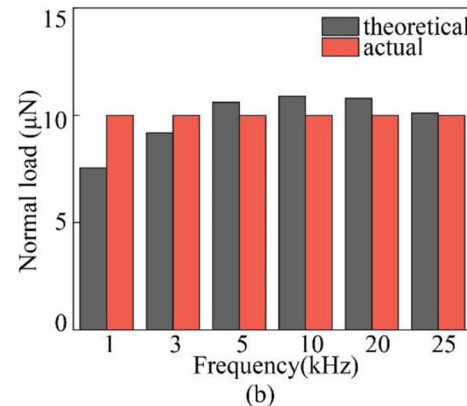
Curve AB represents the instantaneous projective intersection of overlaps region and tip surface in the Z direction. Curve A_1B_1 is the projective intersection of overlap regions and trajectory of P_i period in the Z direction. Curve A_2B_2 is the projective intersection of overlap region and trajectory of P_{i+1} period in the Z direction. Their expressions in coordinate $X_tO_tY_t$ are shown as follows:

$$\begin{aligned} AB : y^2 &= -2(\Delta_t - A - A \sin \theta)x - (A - \Delta_t + A \sin \theta)^2 \\ A_2B_2 : (y - A \cos \theta)^2 &= -2\Delta_t x + \Delta_t^2 - 2\Delta_t A \sin \theta \\ A_1B_1 : (y - A \cos \theta + vT)^2 &= -2\Delta_t x + \Delta_t^2 - 2\Delta_t A \sin \theta \end{aligned} \quad (27)$$

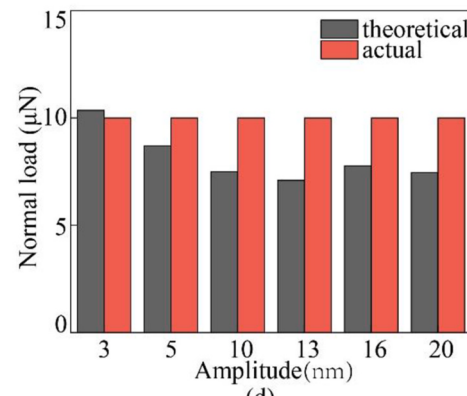
Table 3

Scratching parameters of single groove machining.

Speed (v)	Normal load (F_v)	Amplitude (A)	Frequency (f)
3 $\mu\text{m}/\text{s}$	10 μN	20 nm	20 kHz



(b)



(d)

Fig. 8. Scratching results of different vibration parameters: (a) result of group 1, (b) comparison of theoretical and actual normal load of group1, (c) result of group 2, (d) comparison of theoretical and actual normal load of group2.

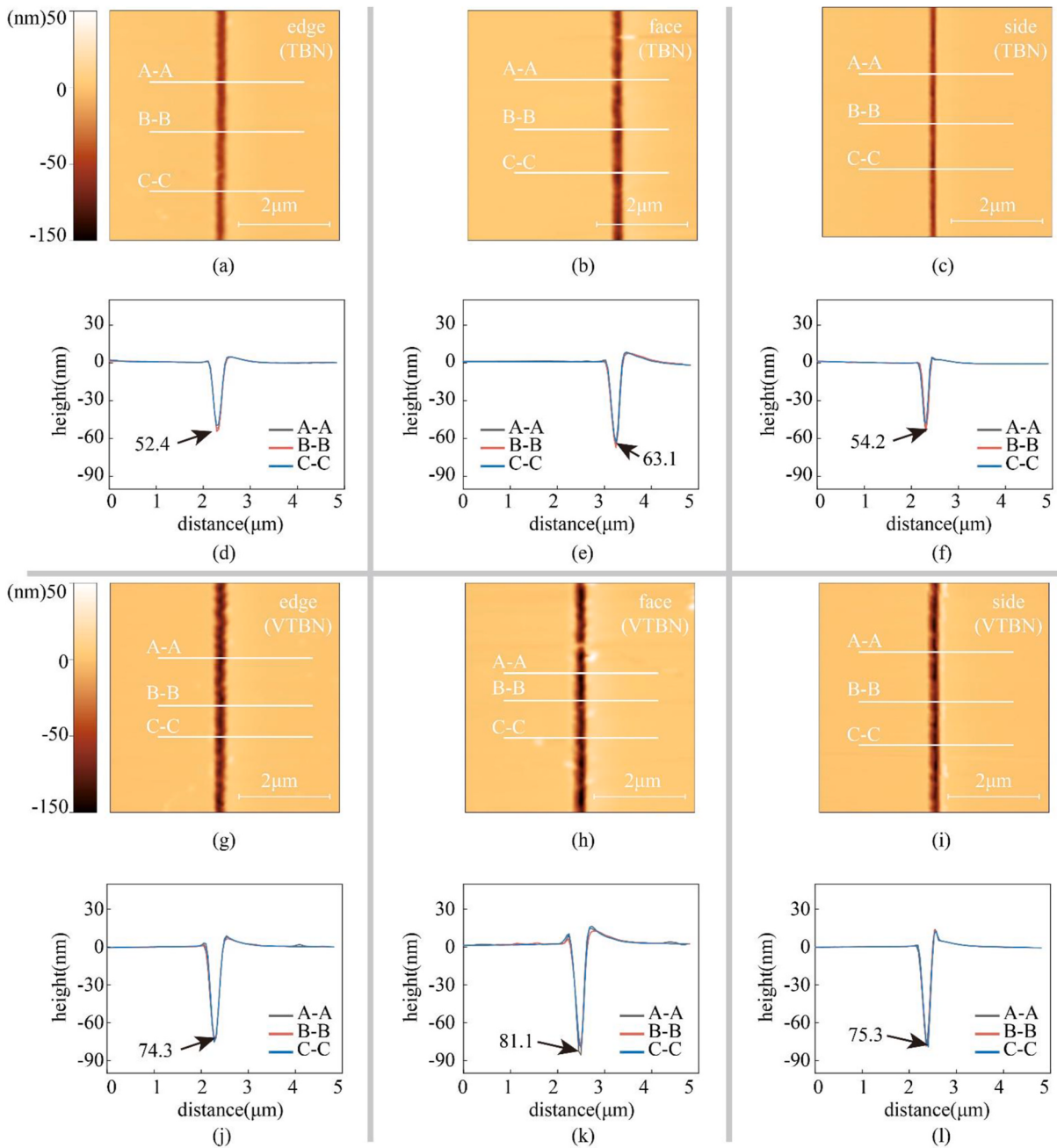


Fig. 9. Experiment results of TBN and VTBN in different directions: (a) TBN in the edge direction, (b) TBN in the face direction, (c) TBN in the side direction, (d) section profile of (a), (e) section profile of (b), (f) section profile of (c), (g) VTBN in the edge direction, (h) VTBN in the face direction, (i) VTBN in the side direction, (j) section profile of (g), (k) section profile of (h), (l) section profile of (i).

In order to calculate the normal contact area in all three stages, the critical positions of three stages need to be determined first. Tip position is indicated by θ , as shown in Fig. 3 (l), which is the local enlarged view of Fig. 3 (h). The critical position between first and second stage is shown in Fig. 3 (j), in which time the value of θ is denoted by θ_1 . P_2 represents the intersection of tip surface and boundary of P_i , which coincide with A when θ equals to θ_1 . The critical position between second and third stage is shown in Fig. 3 (k), in which time the value of θ is denoted by θ_2 . P_1 represents the intersection of tip surface and boundary of P_{i+1} period, which coincide with B when θ equals to θ_2 . Coordinate of P_1 and P_2 in $X_tO_tY_t$ are denoted as (P_{1x}, P_{1y}) and (P_{2x}, P_{2y}) . The critical position of P_1 and P_2 in $X_sO_sY_s$ are denoted as P_1' (P_{1x}', P_{1y}') and P_2' (P_{2x}', P_{2y}'), which is shown in Fig. 3 (j) and Fig. 3 (k). P_{2x}' equals to P_{1x}' , which can be expressed as follows:

$$P'_{1x} = P'_{2x} = \Delta - A - R \quad (28)$$

(P_{1x}', P_{1y}') and (P_{2x}', P_{2y}') can be obtained by solving Eqs. (26) and (28). Then, θ_1 , θ_2 can be calculated as follows:

$$\begin{cases} \theta_1 = \arctan\left(-\frac{P'_{2x}}{P'_{2y}}\right) - \arccos\left(\frac{P_{2x}^2 + P_{2y}^2 + A^2 - R^2}{2A\sqrt{P_{2x}^2 + P_{2y}^2}}\right) + \pi \\ \theta_2 = \arctan\left(-\frac{P'_{1x}}{P'_{1y}}\right) + \pi \end{cases} \quad (29)$$

Normal contact area will be integrated in different stages. For the convenience, $X_tO_tY_t$ coordinate system is employed without further

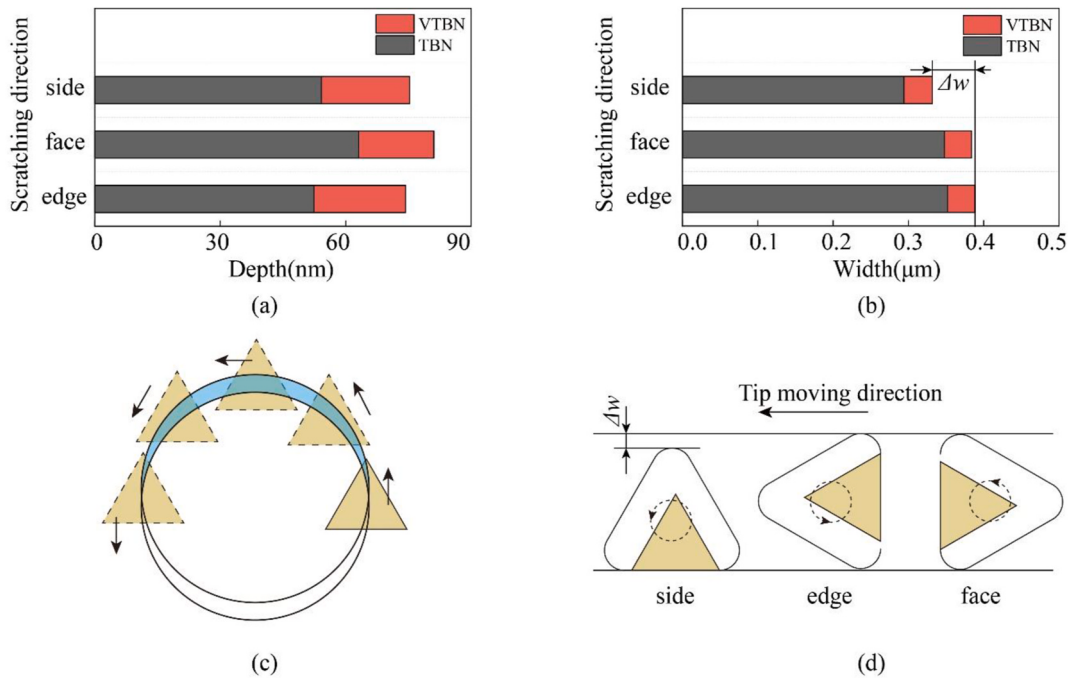


Fig. 10. (a) Residual depth of TBN and VTBN; (b) scratching width of TBN and VTBN; (c) variation of instant cutting direction of VTBN; (d) scratching width of different moving direction in VTBN.

declaration in the following paragraphs.

When $90^\circ \leq \theta < \theta_1$, normal contact area is shown as ABO_t in Fig. 3 (g), where curve AO_t and BO_t is considered as a straight line. Normal contact area can be calculated as follows:

$$A_z = \int_{A_x}^{B_x} \sqrt{-2(\Delta_t - A - A \sin \theta) - (\Delta_t - A - A \sin \theta)^2} dx + \int_0^{A_x} \frac{A_y}{A_x} x dx - \int_0^{B_x} \frac{B_y}{B_x} x dx \quad (30)$$

where (A_x, A_y) and (B_x, B_y) is the x-coordinate of A and B, which can be solved by Eq. (22) (27) and (28).

When $\theta_1 \leq \theta < \theta_2$, normal contact area is shown as ABO_tP_2 in Fig. 3 (h), where curve P_2O_t and BO_t is considered as a straight line. Normal contact area can be calculated as follows:

$$A_z = \int_{A_x}^{B_x} \sqrt{-2(\Delta_t - A - A \sin \theta) - (\Delta_t - A - A \sin \theta)^2} dx + \int_{P_x}^{A_x} \sqrt{R^2 - x^2} dx + \int_0^{P_x} \frac{P_{2y}}{P_{2x}} x dx - \int_0^{B_x} \frac{B_y}{B_x} x dx \quad (31)$$

where A_x can be solved by Eq. (22) (27) and (28). (P_{2x}, P_{2y}) is the coordinate of P_2 , which can be expressed as follows:

$$\begin{bmatrix} P_{2x} \\ P_{2y} \end{bmatrix} = \begin{bmatrix} (A + R)\cos(\alpha + \beta) - A \sin \theta \\ (A + R)\sin(\alpha + \beta) + A \cos \theta - vT \end{bmatrix} \quad (32)$$

where α and β can be calculated as follows:

$$\left\{ \begin{array}{l} \alpha = \arctan\left(\frac{-A \cos \theta + vT}{A \sin \theta}\right) \\ \beta = \arccos\left(\frac{l^2 + (A + R)^2 - R^2}{2l(A + R)}\right) \end{array} \right. \quad (33)$$

where l represents the distance between the center of tip and P_i period trajectory, as shown below:

$$l = \sqrt{v^2 T^2 + A^2 - 2vTA \cos \theta} \quad (34)$$

When $\theta_2 \leq \theta < 270^\circ$, normal contact area can be calculated as follows:

$$A_z = \int_{P_{2x}}^{P_{1x}} \sqrt{R^2 - x^2} dx + \int_0^{P_{2x}} \frac{P_{2y}}{P_{2x}} dx - \int_0^{P_{1x}} \frac{P_{1y}}{P_{1x}} dx \quad (35)$$

Normal load can be obtained according to Eq. (1). A flow chart of the procedure to calculate normal contact area is shown in Fig. 4.

3. Experiment setup

A self-built nanofabrication system is employed to conduct VTBN experiments, which consists of a tip feed system, a 3 degrees of freedom (DOF) platform, a vibrating platform, and some ancillary equipments, as shown in Fig. 5 (a). Scratching trajectory is generated by Simulink and implemented by a dSPACE control board (DS1103). 3-DOF platform is driven by a voltage amplifier (MDT693A, Thorlabs). Motion range in the x , y , z directions is 177.3 μm , 179.3 μm and 17.5 μm respectively. Vibration signal is generated by a waveform generator (33500B, Agilent) and amplified by a high voltage amplifier (ATA-2082 Aigtek). Maximum amplitude and frequency of vibration platform can reach to 50 nm and 25 kHz, which is calibrated by laser doppler vibrometer (OptoMET digital LDV Vector-Series). Polished silicon with the surface roughness R_a of less than 1 nm is employed as the workpiece sample. Scratching direction is coincident with $<100>$ crystal orientation, which is shown in Fig. 5 (b). Scratching depth is set to less than 100 nm to avoid brittle fracture [35]. Indenter is purchased from SYNTON-MDP (Cubenorner, diamond) with a face angle equals to 35.26° as shown in Fig. 5 (c). Indenter is fixed on a cross-shaped cantilever with a rigidity of 0.0031 N/m and the deformation of cantilever is detected by a capacitive sensor (CPL 290, C0.8, Lion Precision, America). Workpiece is cleaned in acetone by ultrasonic immediately after scratching to remove chips and then scanned by an AFM (CPSM 5500, Being) in contact mode. Further details of machining system were introduced in previous study [36].

Scratching procedure is in the following sequence:

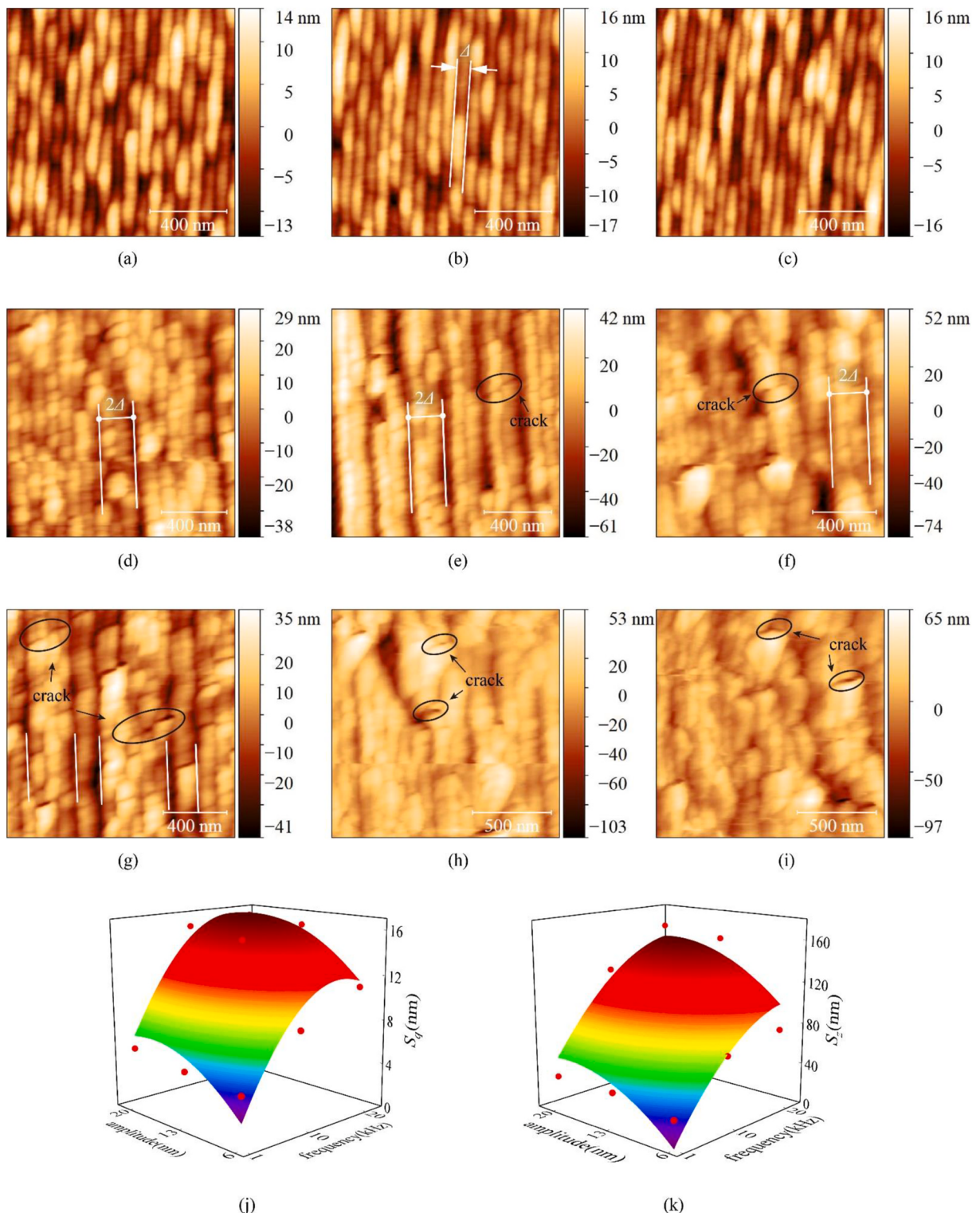


Fig. 11. AFM scanning result of machined surface: (a) 1 kHz, 6 nm, (b) 1 kHz, 13 nm, (c) 1 kHz, 20 nm, (d) 10 kHz, 6 nm, (e) 10 kHz, 13 nm, (f) 10 kHz, 20 nm, (g) 20 kHz, 6 nm, (h) 20 kHz, 13 nm, (i) 20 kHz, 20 nm, (j) effect of vibration parameter on S_q , (k) effect of vibration parameter on S_z .

- Adjust the manual platform to make sure the distance between indenter tip and workpiece is less than 10 μm .
- Turn on the signal generator and apply the vibration on workpiece.
- 3-DOF platform move upwards to drive the workpiece close to indenter until the deformation of cantilever reaches to the pre-set value. Then, z-stage is controlled to make sure deformation remain stable during next step.

- Drive the 3-DOF platform in the x-y direction to conduct 1D groove scratching process.
- 3-DOF platform moves downwards to drive the workpiece away from indenter. A 1D groove scratching process ended.
- Move 3-DOF platform a step of Δ along the x (or y) direction, then repeat step 3–5 to create a 2D surface.

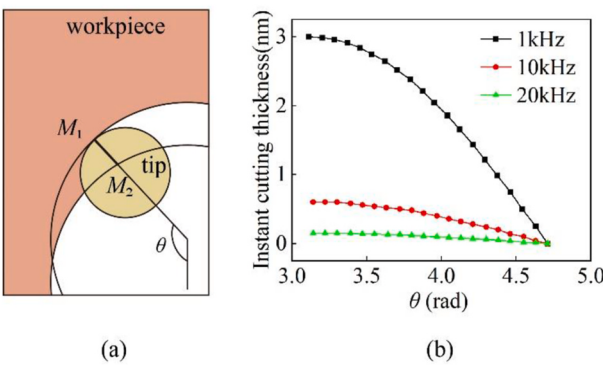


Fig. 12. (a) Instantaneous cutting thickness, (b) Instantaneous cutting thickness of different frequencies ($A = 6 \text{ nm}$).

4. Results and discussion

4.1. Normal load validation

This section will validate the established theoretical normal load model based on the experiment results. In order to investigate the influence of vibration parameter on the contact area during VTBN, different combinations of amplitude and frequency are analyzed. Material removal process of single groove scratching is considered only when \$\theta\$ lies between \$\theta_1\$ to \$\theta_3\$, as shown in Fig. 6 (a). Instantaneous normal contact area increases with \$\theta\$ at first and then decreases. It reaches to the maximum value when \$\theta\$ is about 2.5–3 rad. Higher amplitude and frequency can reduce instantaneous contact area and improve cutting force. As the actual normal load is a constant in machining process, a new statistic indicator of contact area is adopted to predict the normal load instead of instantaneous contact area, which is defined as effective normal contact area, as shown below:

$$A_{z\text{effective}} = \sqrt{\frac{1}{\theta_3 - \theta_1} \int_{\theta_1}^{\theta_3} A_z^2 d\theta} \quad (36)$$

where \$A_{z\text{effective}}\$ represents the effective normal contact area, which is shown in Fig. 6 (b), \$A_z\$ is the instantaneous normal contact area. \$A_{z\text{average}}\$ reaches to \$2853 \text{ nm}^2\$ when vibration amplitude and frequency is 1 nm and 1 kHz respectively. It reduces to \$180 \text{ nm}^2\$ when vibration amplitude and frequency is 20 nm and 20 kHz, which is merely 6.3 % of that in the first situation.

In a 2D surface machining, Material removal process is only considered only when \$\theta\$ lies between \$\theta_1\$ and \$\theta_3\$, as shown in Fig. 6 (c). Instantaneous normal contact area increases with \$\theta\$ at first and then decreases. It reaches to the maximum value when \$\theta\$ is about 3–3.5 rad, which is 15~48 % percent larger than that of 1D groove machining process. Higher amplitude and frequency can reduce instantaneous contact area and improve cutting force in 2D surface machining. \$A_{z\text{average}}\$ of different vibration parameter is shown in Fig. 6 (d). When vibration frequency and amplitude increase from 10 kHz to 10 nm to 20 kHz and 20 nm, \$A_{z\text{average}}\$ reduces from \$228 \text{ nm}^2\$ to \$115 \text{ nm}^2\$. It turns out that VTBN can reduce the contact area and cutting force compared with conventional scratching.

Two groups of experiments are conducted to validate the force model in 1D groove and 2D surface scratching. Machining parameters are shown in Table 1 and experiment results are shown in Fig. 7 (a) and (d). Profiles of section A-A, B-B, C-C are extracted as shown in Fig. 7 (b) and (e). Average depth of 1D groove and 2D surface is measured in a sample length of 3 \$\mu\text{m}\$, which is about 75 nm and 80 nm respectively. It is noted that measured depth in Fig. 7 (b) and (e) is residual depth after elastic recovery. The relation between residual depth and machining depth can be expressed as follows [37,38]:

$$\frac{h_m^k - h_r^k}{h_m} = \left(\frac{6\pi(1 - \sigma^2)\sqrt{r}}{8\sqrt{2}} \right) \frac{H}{E} \quad (37)$$

where \$h_m\$ is machining depth, \$h_r\$ is residual depth, \$k\$ is constant which is relative to indenter shape, \$\sigma\$ is poisson's ratio, \$r\$ is tip radius, \$H\$ is hardness, \$E\$ is elastic modulus. Machining depth can be obtained by substituting \$h_r\$ into Eq. (37). Then, normal load can be calculated according to Eq. (1). Theoretical force and experimental force are shown in Fig. 7 (c) and (f). Theoretical instantaneous and effective normal load is represented by blue squared symbolic lines and blue solid lines respectively. Experimental normal load is represented by red solid lines. During VTBN process, applied normal force is set as a constant under a closed-loop control. Since the vibration frequency of sample is much higher than the resonant frequency of tip suspension system, the tip can be considered as dynamic frozen state despite of the influence of sample vibration [31]. Machining depth is also a constant due to the dynamic frozen state of tip. But instantaneous contact area varies with \$\theta\$, theoretical normal load is also changing according to Eq. (1), which can't be utilized to compare with experimental applied normal load directly. Instead, effective normal load is chosen to validate the force model. During 1D groove machining, theoretical effective normal load is 9.1 \$\mu\text{N}\$, which is 9 % less than the actual normal load. While in 2D surface machining, theoretical effective normal load is 7.8 \$\mu\text{N}\$, which is 22 % less than the actual normal load. The difference can be attribute to the material accumulates, pile-up exists at both side of the machined region, which will increase the contact area and actual normal load. 2D surface machining will result in more materials accumulation, as shown in Fig. 7 (b) and (e), which increases the prediction error in 2D surface machining.

To further investigate the applicable range of the normal load model, more vibration parameters are employed to conduct scratching experiment. Machining parameters are shown in Table 2. Machining and calculating procedure were as follows:

- (1) Scratching process is conducted with the parameters listed in Table 2. Applied normal load is controlled at 10 \$\mu\text{N}\$ by negative feedback method.
- (2) Machining surface is cleaned by ultrasonic cleaning and then scanned by AFM.
- (3) Average residual depth (\$h_r\$) is calculated based on a sample length of 3 \$\mu\text{m}\$ in the stable processing stage.
- (4) Machining depth (\$h_m\$) is calculated based on average residual depth (\$h_r\$) and Eq. (37).
- (5) Theoretical normal load is calculated according to machining depth (\$h_m\$) and Eq. (1) and Eq. (21).

The results are shown in Fig. 8. Theoretical normal load is denoted by black histogram in Fig. 8 (b) and (d). Actual applied normal load is set to 10 \$\mu\text{N}\$. Prediction errors decreased with frequency rising, as shown in Fig. 8 (b). Tip is assumed to be at a dynamic frozen state at a high frequency, lower vibration frequency will lead to an erratic state of tip due to the low rigidity system, which will result in a larger model error. Prediction error is less than 10 % within the frequency range from 3 kHz to 25 kHz. Prediction errors increased with amplitude rising. It reaches to the maximum (29 %) when amplitude is 13 nm. One possible reason might be that higher amplitude leads to higher material accumulate, which will increase the normal contact area and reduce the prediction error. Another possible reason is that higher amplitude will result in a higher stain rate, which will lead to a higher contact stress and make the normal load larger in actual scratching process [39,40].

4.2. Effects of scratching direction on cutting depth and width

Since scratching direction is not considered in the normal load model, the effect of scratching direction will be analyzed via an exper-

ment investigation. Scratching parameters are listed in Table 3. Experiment results are shown in Fig. 9. Scratching results in the edge, face, and side directions without vibration is shown in (a), (b) and (c) respectively. Sections A-A, B-B, C-C are chosen in three arbitrary positions of single groove, whose profiles are shown in (d), (e), and (f). Scratching results of VTBN in the edge, face, side direction are shown in (g), (h) and (i) with their section profiles extracted in (j), (k), and (l) accordingly. Average depth in a sample length of 3 μm is adopted as final residual depth, which is 52.4 nm, 63.1 nm, 54.2 nm in the edge, face, and side direction respectively in TBN process. While final residual depth of VTBN in the edge, face, and side direction is 74.3 nm, 81.1 nm, 75.3 nm respectively, as shown in Fig. 10 (a). Residual depth is quite close in the edge and side direction and reaches to the maximum in the face direction in both TBN and VTBN process. VTBN can enhance the machine ability compared with TBN process, which improves cutting depth by 29 %, 22 % and 28 % in the edge, face, and side direction respectively. During VTBN process, instantaneous scratching direction is changing all the time, three scratching directions exist in every cycle of vibration, which will reduce the influence of scratching directions. Residual depth difference is about 16.9 % in TBN process while 8.4 % in VTBN process. Scratching in the face direction during VTBN will bring in the other two instantaneous scratching directions in VTBN as shown in Fig. 10 (c), while scratching in the side direction and edge direction will lead to lower cutting depth, so cutting depth improvement of VTBN in the face direction is less conspicuous than the other two directions. VTBN can also improve groove width as shown in Fig. 10 (b). Groove width is about 42 nm larger than that of TBN process, which is close to the twice of vibration amplitude. Scratching in the side direction leads to the least groove width due to the asymmetry of tip geometry, groove width can be estimated by following equation:

$$\begin{cases} \text{side direction : } w = 3h_m \tan(\theta_f) + 2A \\ \text{face/edge direction : } w = 2\sqrt{3}h_m \tan(\theta_f) + 2A \end{cases} \quad (38)$$

where w is groove width in the sample surface, h_m is the machining depth which can be obtained by Eq. (37), θ_f is the face angle of indenter, A is vibration amplitude. Estimate error is less than 7 %.

4.3. Influences of machining parameters on surface quality

Surface quality is another major indicator of machining process. Thus, further experiments are conducted to investigate the influence of vibration parameters on surface quality. Amplitude is set as 6 nm, 13 nm and 20 nm and frequency is set as 1 kHz, 10 kHz, 20 kHz. Other parameters are identical with Table 1. Machined surface is scanned by AFM, which is shown in Fig. 11. Surface quality will be discussed from three aspects, i.e., S_q and S_z , microstructures, cracks, where S_q and S_z is defined as follows:

$$\begin{aligned} S_q &= \sqrt{\frac{1}{A} \iint_A (z(x, y) - \bar{z})^2 dx dy} \\ S_z &= |\max(z(x, y)) - \min(z(x, y))| \end{aligned} \quad (39)$$

where $z(x, y)$ is the surface depth at point (x, y) , \bar{z} is the average surface depth, A is measured area.

When frequency is 1 kHz, surface roughness is the best within all frequency range. S_q varies from 4.5 nm to 5.6 nm with vibration amplitude increasing from 6 nm–20 nm, S_z increased from 27 nm to 33 nm accordingly. When frequency increase to 10 kHz, surface roughness rises rapidly, S_q varies from 8.5 nm to 16 nm and S_z varies from 67 nm to 126 nm with amplitude increases. When frequency reaches to 20 kHz, S_q varies from 11.2 nm to 16.4 nm and S_z varies from 76 nm to 162 nm with amplitude increasing. Surface roughness is almost stable when frequency is larger than 10 kHz. Frequency has more influence on surface roughness than amplitude. Micro structure of the machined surface is

also different at different machining parameters. Machining procedure of 2D surface is composed of many repeated grooves scratching, which can be considered as periodic ripples in a wavelength of Δ , as shown in Fig. 11 (a)–(c). When frequency reaches to 10 kHz, the micro structure converts to a new type, groove depth alternates between shallow and deep. The distance between two deep grooves is about two times of Δ . When frequency increases to 20 kHz, the microstructure changes again, the distance between two deep grooves is erratic, varying around several times of Δ , as shown in Fig. 11 (e). These micro structures are destroyed when amplitude is larger than 13 nm. This phenomenon can be attributed to the decrease of instantaneous cutting thickness, which is represented by $M_1 M_2$ in Fig. 12 (a). Material removal procedure mainly exists when θ is larger than π according to Fig. 6, so the instantaneous cutting thickness is only considered when θ is larger than π . Only the effect of frequency is present because the influence of amplitude is negligible compared with that of frequency. Material removal mechanism transforms from cutting effect to ploughing and squeezing in the frequency of higher than 10 kHz, which is harmful to the machined surface and makes the machined surface worse. When frequency increases to 20 kHz, instantaneous cutting depth decreased rapidly. Higher frequency will also introduce cracks, as shown in Fig. 11 (e)–(i). Crack usually starts from previous deep groove and ends in the next deep groove. Higher frequency and amplitude will result in a relatively larger material strain rate during scratching, which will increase the stress of material and introduce cracks of machined surface [41]. Besides, higher frequency leads to a relatively larger vibration speed, which will also increase the transition from ductile to brittle mode during material process [42]. To sum up, the introduction of vibration may improve scratching efficiency but also cause a worse machined surface.

5. Conclusion

A theoretical model of normal load during VTBN is established in both groove machining and 2D surface machining. Instantaneous normal load and effective normal load are analyzed in different vibration parameters based on the proposed model. To validate the applicable range of this model, a series of experiments is conducted on a self-built nanofabrication system. Furthermore, scratching depth, groove width and surface quality are thoroughly analyzed based on the experiments. Conclusions are drawn as follows:

- A scratching depth model of VTBN is established and effective contact area is first proposed to predict scratching depth based on scratching force and vibration parameters. This model can reduce prediction error of the instantaneous scratching depth model and has a better effect. Prediction errors of normal load are less than 30 % in the whole range and reaches the maximum at the highest amplitude. Errors can be attributed to the simplification of indenter, material accumulate and increase of contact stress in high strain rate.
- Theoretical results show that effective contact area reduced more in higher frequency and larger amplitude. Increase of frequency and amplitude make a similar contribution to the reduction of normal load. This model provides theoretical support for better understanding of mechanism in VTBN.
- Inconsistency of scratching depth in different scratching directions is improved in VTBN compared to conventional scratching, which reduces from 16.9 % to 8.4 % with the addition of vibration. Groove width is also wider in higher amplitude, which is equal to the twice of amplitude.
- Vibration parameters have a significant influence on surface quality. Higher frequency and larger amplitude lead to a smaller cutting thickness and higher strain rate, resulting in a worse machined surface. Excessive large amplitude will harm the micro structures on machined surface and lead to tiny fractures.

CRediT authorship contribution statement

Weijie Wang: Writing – review & editing, Writing – original draft, Software, Methodology. **Guanghui Zhao:** Writing – review & editing, Writing – original draft. **Yanling Tian:** Funding acquisition, Conceptualization. **Zhilai Lu:** Validation. **Hui Tang:** Visualization, Funding acquisition. **Fujun Wang:** Resources. **Dawei Zhang:** Resources.

Declaration of competing interest

The authors declare that they have no known competing financial interests or personal relationships that could have appeared to influence the work reported in this paper.

Data availability

Data will be made available on request.

Acknowledgements

The authors would like to thank the financial support from National Natural Science Foundation of China (52075364, 52205506), the Project of State Key Laboratory of Precision Manufacturing for Extreme Service Performance, Central South University (ZZYJKT2023-09), the Guangdong INTERNATIONAL COOPERATION Program of Science and Technology (2022A0505050078), the Open Fund of State Key Laboratory of Precision Electronic Manufacturing Technology and Equipment, Guangdong University of Technology (JMDZ2021001).

References

- [1] M.J. Madou, *Manufacturing Techniques for Microfabrication and nanotechnology* [M], vol. 2, CRC press, 2011.
- [2] S. Gao, H. Huang, Recent advances in micro- and nano-machining technologies, *Front. Mech. Eng.* 12 (1) (2017) 18–32, <https://doi.org/10.1007/s11465-017-0410-9>.
- [3] F.J. Wang, B.C. Shi, Z.C. Huo, et al., Control and dynamic releasing method of a piezoelectric actuated microgripper, *Precision Engineering-Journal of the International Societies for Precision Engineering and Nanotechnology* 68 (2021) 1–9, <https://doi.org/10.1016/j.precisioneng.2020.10.014>.
- [4] J. Jeon, H.C. Floresca, M. Kim, Fabrication of complex three-dimensional nanostructures using focused ion beam and nanomanipulation, *Journal of Vacuum Science & Technology B, Nanotechnology and Microelectronics: Materials, Processing, Measurement, and Phenomena* 28 (3) (2010) 549–553, <https://doi.org/10.1116/1.3406134>.
- [5] J. Ran, O. Dyck, X. Wang, et al., Electron-Beam-related Studies of Halide perovskites: challenges and opportunities, *Adv. Energy Mater.* 10 (26) (2020), <https://doi.org/10.1002/aenm.201903191>.
- [6] M. Huff, Recent advances in reactive ion etching and applications of high-aspect-ratio microfabrication, *Micromachines* 12 (8) (2021), <https://doi.org/10.3390/mi12080991>.
- [7] L. Wu, P. Chen, L. Deng, et al., Effects of crystal planes on topography evolution of silicon surface during nanoscratch-induced selective etching, *Mater. Sci. Semicond. Process.* 124 (2021) 105606, <https://doi.org/10.1016/j.jmssp.2020.105606>.
- [8] H. Hu, H.J. Kim, S. Somnath, Tip-based nanofabrication for scalable manufacturing, *Micromachines* 8 (3) (2017) 90, <https://doi.org/10.3390/mi8030090>.
- [9] S. Xu, T. Kuriyagawa, K. Shimada, et al., Recent advances in ultrasonic-assisted machining for the fabrication of micro/nano-textured surfaces, *Front. Mech. Eng.* 12 (1) (2017) 33–45, <https://doi.org/10.1007/s11465-017-0422-5>.
- [10] Y. He, W. Tang, P. Gao, et al., Nano-polishing characteristics in vibration-assisted CMP of single-crystal silicon carbide via molecular dynamics simulations, *Mater. Sci. Semicond. Process.* 164 (2023) 107637, <https://doi.org/10.1016/j.jmssp.2023.107637>.
- [11] W. Lin, Z. Hu, Y. Chen, et al., Comparison of vibration-assisted scratch characteristics of SiC polytypes (3C-, 4H- and 6H-SiC), *Micromachines* 13 (4) (2022), <https://doi.org/10.3390/mi13040640>.
- [12] Y. Chen, Z. Hu, J. Jin, et al., Molecular dynamics simulations of scratching characteristics in vibration-assisted nano-scratch of single-crystal silicon, *Appl. Surf. Sci.* 551 (2021), <https://doi.org/10.1016/j.apsusc.2021.149451>.
- [13] Z. Qiu-Yang, Z. Zhen-Yu, D. Cong, et al., Mechanical response of single-crystal copper under vibration excitation based on molecular dynamics simulation, *J. Manuf. Process.* 75 (2022) 605–616, <https://doi.org/10.1016/j.jmapro.2021.11.066>.
- [14] Y.-H. Lee, K.-L. Wu, J.-H. Jhou, et al., Two-dimensional vibration-assisted magnetic abrasive finishing of stainless steel SUS304, *Int. J. Adv. Des. Manuf. Technol.* 69 (9–12) (2013) 2723–2733, <https://doi.org/10.1007/s00170-013-5242-0>.
- [15] C. Jian-Hao, Z. Qiu-Yang, Z. Zhen-Yu, et al., Molecular dynamics simulation of monocrystalline copper nano-scratch process under the excitation of ultrasonic vibration, *Mater. Res. Express* 8 (4) (2021), <https://doi.org/10.1088/2053-1591/abf2eb>.
- [16] Y. He, J. Zhang, W. Zhou, et al., Study on force reduction mechanism in ultrasonic-assisted grinding based on single-grain scratching, *Arch. Civ. Mech. Eng.* 22 (2) (2022), <https://doi.org/10.1007/s43452-022-00399-4>.
- [17] W. Zheng, D. Qu, G.C. Qiao, Multi-phase modeling of SiC particle removal mechanism in ultrasonic vibration-assisted scratching of SiCp/Al composites, *Int. J. Adv. Manuf. Technol.* 113 (1–2) (2021) 535–551, <https://doi.org/10.1007/s00170-021-06675-6>.
- [18] Y. Gu, Y. Zhou, J. Lin, et al., Analytical prediction of subsurface damages and surface quality in vibration-assisted polishing process of silicon carbide ceramics, *Materials* 12 (10) (2019), <https://doi.org/10.3390/ma12101690>.
- [19] M. Versen, B. Klehn, U. Kunze, et al., Nanoscale devices fabricated by direct machining of GaAs with an atomic force microscope, *Ultramicroscopy* 82 (1) (2000) 159–163, [https://doi.org/10.1016/S0304-3991\(99\)00127-8](https://doi.org/10.1016/S0304-3991(99)00127-8).
- [20] F. Iwata, M. Yamaguchi, A. Sasaki, Nanometer-scale layer modification of polycarbonate surface by scratching with tip oscillation using an atomic force microscope, *Wear* 254 (10) (2003) 1050–1055, [https://doi.org/10.1016/s0043-1648\(03\)00311-9](https://doi.org/10.1016/s0043-1648(03)00311-9).
- [21] K.K. Lu, Y.L. Tian, C.F. Liu, et al., Experimental investigation of the effects of vibration parameters on ultrasonic vibration-assisted tip-based nanofabrication, *Int. J. Mech. Sci.* 198 (2021) 106387, <https://doi.org/10.1016/j.ijmecsci.2021.106387>.
- [22] C. Li, F. Zhang, B. Meng, et al., Material removal mechanism and grinding force modelling of ultrasonic vibration assisted grinding for SiC ceramics, *Ceram. Int.* 43 (3) (2017) 2981–2993, <https://doi.org/10.1016/j.ceramint.2016.11.066>.
- [23] F. Zheng, Z. Dong, R. Kang, et al., Analysis of material removal behavior in ultrasonically assisted scratching of RB-SiC from energy aspects, *Int. J. Adv. Des. Manuf. Technol.* 98 (9–12) (2018) 2257–2270, <https://doi.org/10.1007/s00170-018-2256-7>.
- [24] X. Kong, P.H. Cohen, J. Dong, Predictive modeling of feature dimension for tip-based nano machining process, *J. Manuf. Process.* 24 (2016) 338–345, <https://doi.org/10.1016/j.jmapro.2016.06.013>.
- [25] Y. Feng, F.-C. Hsu, Y.-T. Lu, et al., Surface roughness prediction in ultrasonic vibration-assisted milling. *Journal of Advanced Mechanical Design, Systems, and Manufacturing* 14 (4) (2020) JAMDSM0063, <https://doi.org/10.1299/jamdsm.2020jamdsm0063>. JAMDSM0063.
- [26] Y. Feng, F.-C. Hsu, Y.-T. Lu, et al., Force prediction in ultrasonic vibration-assisted milling, *Mach. Sci. Technol.* 25 (2) (2020) 307–330, <https://doi.org/10.1080/10910344.2020.1815048>.
- [27] J. Cao, Y. Wu, D. Lu, et al., Material removal behavior in ultrasonic-assisted scratching of SiC ceramics with a single diamond tool, *Int. J. Mach. Tool Manufact.* 79 (2014) 49–61, <https://doi.org/10.1016/j.ijmachtools.2014.02.002>.
- [28] D.E. Brehl, T.A. Dow, Review of vibration-assisted machining, *Precis. Eng.* 32 (3) (2008) 153–172, <https://doi.org/10.1016/j.precisioneng.2007.08.003>.
- [29] F. Jiao, B. Zhao, C.S. Liu, et al., Material removal rate characteristics in ultrasonic aided lapping of engineering ceramics based on single-point scratch, *Key Eng. Mater.* 375–376 (2008) 263–267. <https://doi.org/10.4028/www.scientific.net/KEM.375-376.263>.
- [30] Y. Geng, Y. Yan, Y. Zhuang, et al., Effects of AFM tip-based direct and vibration assisted scratching methods on nanogrooves fabrication on a polymer resist, *Appl. Surf. Sci.* 356 (2015) 348–354, <https://doi.org/10.1016/j.apsusc.2015.08.068>.
- [31] L. Zhang, J. Dong, P.H. Cohen, Material-insensitive feature depth control and machining force reduction by ultrasonic vibration in AFM-based nanomachining, *IEEE Trans. Nanotechnol.* 12 (5) (2013) 743–750, <https://doi.org/10.1109/TNANO.2013.2273272>.
- [32] S. Heamawatanachai, E. Bamberg, Cutting force model of orbital single-point micromachining tool, *Int. J. Mach. Tool Manufact.* 50 (9) (2010) 815–823, <https://doi.org/10.1016/j.ijmachtools.2010.05.002>.
- [33] J. Wang, Y. Yan, Z. Li, et al., Towards understanding the machining mechanism of the atomic force microscopy tip-based nanomilling process, *Int. J. Mach. Tool Manufact.* 162 (2021), <https://doi.org/10.1016/j.ijmachtools.2021.103701>.
- [34] F.P. Bowden, F.P. Bowden, D. Tabor, *The Friction and Lubrication of Solids* [M], vol. 1, Oxford university press, 2001.
- [35] M. Zhou, P. Zhao, Prediction of critical cutting depth for ductile-brittle transition in ultrasonic vibration assisted grinding of optical glasses, *Int. J. Adv. Des. Manuf. Technol.* 86 (5–8) (2016) 1775–1784, <https://doi.org/10.1007/s00170-015-8274-9>.
- [36] Y.L. Tian, K.K. Lu, F.J. Wang, et al., A spatial deployable three-DOF compliant nano-positioner with a three-stage motion amplification mechanism, *Ieee-Asme Transactions on Mechatronics* 25 (3) (2020) 1322–1334, <https://doi.org/10.1109/tmech.2020.2973175>.
- [37] H.P. Kirchner, J.A. Tiracorda, T.J. Larchuk, Elastic recovery at static loading and impact indentations in MgF₂, *J. Am. Ceram. Soc.* 66 (11) (1983) 786–789, <https://doi.org/10.1111/j.1151-2916.1983.tb10563.x>.
- [38] P.Z. Wang, P.Q. Ge, Z.Q. Li, et al., A scratching force model of diamond abrasive particles in wire sawing of single crystal SiC, *Mater. Sci. Semicond. Process.* 68 (2017) 21–29, <https://doi.org/10.1016/j.jmssp.2017.05.032>.
- [39] X. Yang, Z. Qiu, C. Lu, et al., Modelling the strain rate sensitivity on the subsurface damages of scratched glass ceramics, *Ceram. Int.* 43 (15) (2017) 12930–12938, <https://doi.org/10.1016/j.ceramint.2017.06.191>.
- [40] Z. Rongtao, W. Xian, L. Chaoyong, et al., Strain-rate dependence of mechanical behavior and deformation mechanisms in bimodal nanostructured Ni under micro-

- scratch testing, *Mech. Mater.* 121 (2018) 21–30, <https://doi.org/10.1016/j.mechmat.2018.03.005>.
- [41] J.Q. Wang, Y.Q. Geng, Z.H. Li, et al., Study on the vertical ultrasonic vibration-assisted nanomachining process on single-crystal silicon, *Journal of Manufacturing Science and Engineering-Transactions of the Asme* 144 (4) (2022) 11, <https://doi.org/10.1115/1.4052356>.
- [42] T. Tawakoli, H. Kitzig, R.D. Lohner, Experimental investigation of material removal mechanism in grinding of alumina by single grain scratch test[C], in: 16th International Symposium on Advances in Abrasive Technology (ISAAT 2013), 2013, pp. 96–102. <https://doi.org/10.4028/www.scientific.net/AMR.797.96>.